# Three-photon above-threshold ionization of magnesium

A. Reber,[1] F. Martín,[2] H. Bachau,[3] and R. S. Berry[1]
[1]*Department of Chemistry and The James Franck Institute, The University of Chicago, Chicago, Illinois 60637, USA*
[2]*Departamento de Química C-9, Universidad Autónoma de Madrid, 28049 Madrid, Spain*
[3]*Centre des Lasers Intenses et Applications (UMR 5107 du CNRS), Université de Bordeaux I, 351 Cours de la Libération, F-33405 Talence, France*

(Received 22 June 2003; published 2 December 2003)

Three-photon ionization cross sections from the ground state, and two-photon ionization from the $3\,^1P(3s3p)$ state have been calculated for Mg in the region between the $3p$ and $4s$ ionization thresholds. These processes include an above-threshold ionization process for the last absorbed photon. We have used the Green's-function method in the Feshbach formalism and an $L^2$ close coupling approach, with a basis of $L^2$ integrable *B*-spline functions. We report the positions, widths, and assignments of a number of relevant $^1P^o$ and$^1F^o$ doubly excited Feshbach states. We also observe unusually high cross sections due to a bound-bound transition from the $3\,^1S(3s^2)$ to the $3\,^1P(3s3p)$ state, a core excitation process, and the population of an intermediate doubly excited state. Both total cross sections and angular distributions are reported.

DOI: 10.1103/PhysRevA.68.063401 PACS number(s): 32.80.Rm

## I. INTRODUCTION

Experiments using the photoionization of magnesium as an electron source [1] have motivated our theoretical study in three-photon above-threshold ionization (ATI). ATI is a process in which an atom absorbs more photons than the minimum number required to ionize the atom [2]. The energy may then be transferred either into kinetic energy of the ejected electron, or into exciting the remaining ion. In the cited experiment [1], the photoelectron energy spectra is measured while Mg vapor is exposed to resonant radiation Mg $3\,^1S(3s^2)\rightarrow 3\,^1P(3s3p)$ at the entrance to a magnetic bottle spectrometer (MBS) [3]. This experiment shows two fast electron time-of-flight peaks, along with the expected resonance enhanced two-photon ionization (REMPI) peak. The slower of the two is due to a superelastic collision in which a REMPI electron de-excites a second Mg atom from the $3\,^1P(3s3p)$ to the $3\,^3P(3s3p)$ state. The faster peak was originally ascribed to a three-photon ionization; however, one should be cautious before accepting this as a definitive conclusion. Indeed, one difficulty in these time-of-flight experiments is that the energies of superelastically scattered electrons and of electrons ejected due to multiphoton ionization are identical. Thus there are two processes yielding the highest energy electrons. One is two-photon REMPI, which is followed by the ejected electron superelastically scattering with a second excited Mg atom. In the collision, the atom de-excites from the $3\,^1P(3s3p)$ state to the $3\,^1S(3s^2)$ state. The other is three-photon ionization of Mg, in which the last photon produces a continuum-continuum transition. While the initial power study on the photon intensity seemed to suggest that the process is primarily due to ATI, the measured cross section is unusually high, and saturation of the $3\,^1S(3s^2)\rightarrow 3\,^1P(3s3p)$ transition leaves the answer open to doubt. In principal, a density dependence study should determine the dominant mechanism, however, the density range available to the apparatus makes this method impractical. Furthermore, one peak in the electron spectra occurs at an intermediate energy unaccountable in terms of accepted ATI processes, but is consistent with a superelastic scattering process. It is exceedingly difficult to determine if the appropriate mechanism is ATI or REMPI followed by a superelastic collision experimentally.

In order to facilitate the determination of the mechanism, we have calculated both three-photon ATI from the $3\,^1S(3s^2)$ state and two-photon ATI from the $3\,^1P(3s3p)$ state. The two processes investigated are shown in Fig. 1; process (A), generally referred to as the three-photon process, is a one-color three-photon ionization of Mg from the ground $3\,^1S(3s^2)$ state. Process (B), also referred to as the two-photon process, is a one-color two-photon ionization from the $3\,^1P(3s3p)$ state. The calculation of process (B) simulates a two-color study, in which the $3\,^1S(3s^2)\rightarrow 3\,^1P(3s3p)$ transition is pumped, followed by the one-color two-photon ionization where the photon energy is varied.

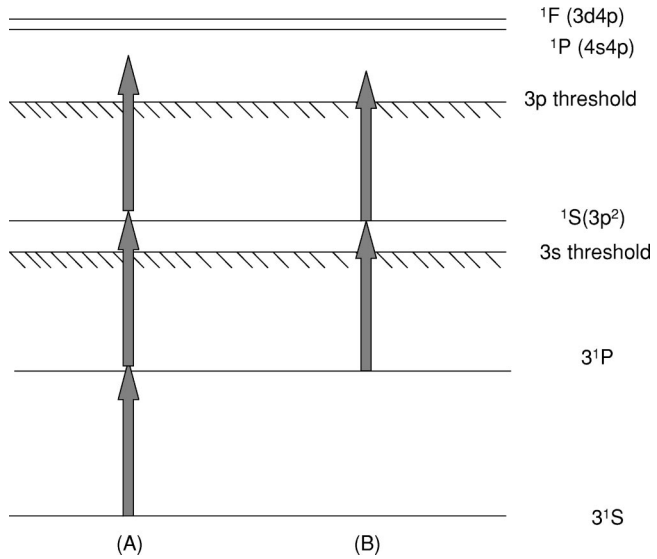


FIG. 1. A sketch of the two processes studied in this paper. (A) is a one-color three-photon process form the ground state. (B) is a one-color two-photon process from the $3\,^1P(3s3p)$ state.

 

ATI is a fundamental process in strong field dynamics that is useful for investigating doubly excited states also referred to as autoionizing states (AIS), shape resonances, and other resonant processes found in the continuum. It also represents a test for our ability to describe continuum state processes. Indeed, in this process, the continuum-continuum transitions are more difficult to evaluate than bound-continuum transitions because the wave functions are not localized, and poles may be present in the intermediate-state Green's function. Our theoretical approach allows us to solve this problem in a simple way and to evaluate the angular distributions of the ejected electrons, which poses an even stricter test for our method [4].

In addition to its use as a tool in recent experiments [1], there is a great deal of intrinsic interest in the ionization properties of Mg [5–15]. Karapanagioti and co-workers have studied population trapping using three-photon ionization in this energy range [12,13]. Bonanno *et al.* and Shao *et al.* have studied doubly excited states in two-photon ionization of Mg [16,17]. Several theoretical studies have also been performed on Mg photoionization. Lyras and Bachau have studied phase control in two- and four-photon ionization in Mg [18]. Chang *et al.* have studied atomic structure effects in three-photon ionization of Mg [14]. Luc-Koenig *et al.* have studied a variety of photoionization properties of Mg, including two-photon ATI [11]. Moccia and Spizzo and Mengali and Moccia studied one- and two-photon ionization of Mg using an $L^2$ integrable basis [5–9]. And, in a previous paper, the authors have studied two-photon ATI in Mg [15]. Despite the attention Mg receives as a convenient target for both experiments and theory, there has yet to be a comprehensive calculation on three-photon ionization in the region of the $3\,^1S(3s^2)$–$3\,^1P(3s3p)$ transition.

In this work, we present total and differential cross sections for three-photon ionization from the ground state and two-photon ionization from the $3\,^1P(3s3p)$ state where the final energy lies above the $3p$ threshold. These processes are diagrammed in Fig. 1. In these cases, it is only the final photon which induces a continuum-continuum transition. These calculations were performed using an $L^2$ integrable *B*-spline basis [19,20]. *B*-splines are a set of piecewise polynomials, which are capable of simultaneously representing bound and continuum states. We will use the Green's-function method in the Feshbach formalism as described by Sánchez and Martín [21], and the $L^2$ close-coupling approach [22]. We work under the assumption of *LS* coupling, and use lowest-order perturbation theory (LOPT). We are also interested in the electronic structure of the Feshbach states, and we describe their positions, widths, and assignments. This method allows for a comprehensive study of the photoionzation properties of Mg, including ATI.

Atomic units are used throughout, unless otherwise noted. When we designate a state by a single configuration, that is the dominant configuration in our calculation.

## II. THEORY

The multiphoton cross sections are evaluated in the dipole approximation for linearly polarized light. The cross section for an *N*-photon ionization process is given by

$$\sigma(\mathrm{cm}^{2N}\,\mathrm{s}^{N-1}) = C^{(N)}\omega^N |M_{g\mu}^{(N)}|^2. \tag{1}$$

$C^{(N)}$ is a conversion from atomic to cgs units, and $C^{(2)}$ is $2.505\,475\times10^{-52}$ cm$^4$ s, $C^{(3)}$ is $7.78\times10^{-87}$ cm$^6$ s$^2$, $\omega$ is the photon energy (a.u.), and $M^{(N)}$ is the amplitude associated with the multiphoton transition between the initial state $g$ and the final channel $\mu$ in atomic units. For the two-photon case, the transition amplitude is found by

$$M_{g\mu}^{(2)} = \sum_{\nu} \frac{\langle g|\mathbf{D}\cdot\mathbf{e}|\nu\rangle\langle\nu|\mathbf{D}\cdot\mathbf{e}|\mu\rangle}{E_g+\omega-E_\nu} + \lim_{\eta\to0^-}\int dE_\nu \frac{\langle g|\mathbf{D}\cdot\mathbf{e}|\nu\rangle\langle\nu|\mathbf{D}\cdot\mathbf{e}|\mu\rangle}{E_g+\omega-E_\nu-i\eta}. \tag{2}$$

Here, $\nu$ represents all possible intermediate (bound and continuum) states, $g$ represents the ground state, **D** is the dipole operator, and **e** is the polarization vector. The three-photon amplitude is given by

$$M_{g\mu}^{(3)} = \lim_{\eta\to0^-}\sum_{\nu_1,\nu_2}\int\int dE_{\nu1}dE_{\nu2} \times \frac{\langle g|\mathbf{D}\cdot\mathbf{e}|\nu_1\rangle\langle\nu_1|\mathbf{D}\cdot\mathbf{e}|\nu_2\rangle\langle\nu_2|\mathbf{D}\cdot\mathbf{e}|\mu\rangle}{(E_g+\omega-E_{\nu1}-i\eta)(E_g+2\omega-E_{\nu2}-i\eta)}. \tag{3}$$

The summation integral symbol describes four terms in the equation, the integral over both $dE_{\nu1}$ and $dE_{\nu2}$, the sum over both $\nu_1$ and $\nu_2$, and the two cross terms. The velocity gauge of the dipole operator is used throughout this calculation. $E_g$ is the energy of the ground state and $E_\nu$, $E_{\nu1}$, and $E_{\nu2}$ are the energies of the intermediate states. Equations (2) and (3) show that if a bound intermediate state lies at the energy $E_g+\omega$ or $E_g+2\omega$, the cross section diverges. This includes the case where $\omega$ resonantly couples with a bound transition in the ionized atom. This means that the cross section for a process in which the resonant $3s\to3p$ transition in $Mg^+$ is pumped, appears to produce a singularity. On initial inspection, it may appear that in the case of ATI we would face a similar problem with poles appearing in the denominator of Eqs. (2) and (3). This is not the case because the integral must be evaluated by surrounding the pole in the complex plane. In the $L^2$ approach, this leads to the evaluation of a discrete summation corresponding to the principal value part of the integral and an imaginary delta term associated with the pole [23]. The discretization is then done by varying the box size to ensure that the energies for the true continuum state associated with the pole and its discrete representation match precisely. The intermediate-state wave functions were calculated using the $L^2$ integrable close coupling method as developed by Cortés and Martín [22]. In this method, the multichannel continuum is transformed into a sum of single-channel continua or orthogonal uncoupled continuum states. The single channels are found by diagonalizing the Hamiltonian in a basis of two electron configurations. For intermediate continuum states, one defines two open channels, $3sks$ and $3skd$, and closed channels associ-

ated with the doubly excited states. These uncoupled continuum states are found by diagonalizing,

$$\left(\sum_{\mu'} P_{\mu'}\mathcal{H}P_{\mu'}-E\right)\zeta_{\mu E}=0, \tag{4}$$

where $\zeta_{\mu E}$ is the uncoupled continuum state, $P_\mu$ is a projection operator which ensures orthogonality between the channels, and $\mu$ represents each channel. The interchannel coupling is introduced using a Lippman-Schwinger formalism. The resulting intermediate continuum state is written

$$\begin{aligned}\Psi^-_{\mu E_{n_\mu}}=\rho_\mu^{1/2}(E_{n_\mu})\Bigg(&\zeta_{\mu n_\mu}+\sum_{\mu' n'_{\mu'}}\sum_{\mu'' n''_{\mu''}}\\&\times\langle\zeta_{\mu' n'_{\mu'}}|G^-(E_{n_\mu})|\zeta_{\mu'' n''_{\mu''}}\rangle\\&\times\langle\zeta_{\mu'' n''_{\mu''}}|V|\zeta_{\mu n_\mu}\rangle\zeta_{\mu' n'_{\mu'}}\Bigg),\end{aligned} \tag{5}$$

$$G^-(E)=\lim_{\eta\to 0^-}\frac{1}{E-\mathcal{H}-i\eta}, \tag{6}$$

$$V=\sum_{\mu\mu',\mu\neq\mu'} P_\mu\mathcal{H}P_{\mu'}, \tag{7}$$

where $\rho_\mu$ is the density of states in a given channel. The Green's-function matrix elements in Eq. (6) may then be solved using algebraic methods, as described in Ref. [22]. The coupling between channels from Eq. (5) is the electron-electron interaction and the polarization potential.

The final continuum states are treated in the Feshbach formalism [24], using the method developed by Sánchez and Martín [21]. In this method, the resonant and nonresonant contributions to the wave functions are treated separately [24]. The nonresonant configurations are selected by the $P$ projection operator, and the doubly excited configurations are selected by the $Q$ operator. This permits the calculation of the widths and positions of the doubly excited states in a single calculation. It also clarifies the role of correlation in the spectra by identifying the Feshbach state, and the weights of the contributing configurations. For each channel $\mu$ the exact continuum wave function can be written as

$$\begin{aligned}|\Psi^-_{\mu E}\rangle=&\frac{\langle\phi_s|QHP|P\Psi^{0^-}_{\mu E}\rangle}{E-\mathcal{E}_s-\Delta_s(E)-i\Gamma_s(E)/2}|\phi_s\rangle\\&+[1+G_Q^{(s)}(E)QHP]\\&\times\Bigg\{|P\Psi^{0^-}_{\mu E}\rangle+\frac{\langle\phi_s|QHP|P\Psi^{0^-}_{\mu E}\rangle}{E-\mathcal{E}_s-\Delta_s(E)-i\Gamma_s(E)/2}\\&\times G_P^{(s)^-}(E)PHQ|\phi_s\rangle\Bigg\},\end{aligned} \tag{8}$$

where $G_Q^{(s)}$ and $G_P^{(s)}$ are the Green's operators associated with their respective space, $|\phi_s\rangle$ is the resonant wave function of energy $\mathcal{E}_s$, $|\Psi^-_{\mu E}\rangle$ is the nonresonant wave function, and $E$ is the energy of the final state; $\mathcal{E}_s$, $\Delta_s(E)$, and $\Gamma_s(E)$ are the exact position, shift, and width of the doubly excited states. The notation explicitly shows that the shift and width are dependent on the energy of the final continuum state. As mentioned above, Eq. (8) is exact and has been used in our evaluation of the $N$-photon matrix element given in Eqs. (2) and (3). The resonance parameters have been obtained by choosing $E=\mathcal{E}_s$, which is the usual approximation in the framework of the Feshbach theory [24].

All necessary wave functions were represented in a basis of two-electron states constructed from a $B$-spline basis [19,20]. $B$-splines are an $L^2$ integrable basis so that this representation results in a discretization of the continuum [25]. For each angular momentum, a basis of 650 $B$-splines of order 10 was placed in a linear knot sequence with the maximum radius of 250 a.u. The order of the basis refers to the number of nonzero basis functions at each radial point, except at the edge of the box where all basis functions are removed which do not conform to the boundary conditions. The basis was large enough that the energy levels and cross sections were essentially invariant to small changes in the size of the box and the basis. The $Mg^{2+}$ core is represented by an analytical model potential that reproduces the valence-core potential resulting from self-consistent calculations, plus a phenomenological potential that represents polarization of the core. Details of this model potential can be found in Moccia and Spizzo [26]. The one-electron states are found by diagonalizing the $Mg^+$ Hamiltonian using the above $B$-spline basis set; this diagonalization is performed by imposing orthogonality with the core. The two-electron states included in Eqs. (4), (5), and (6) were evaluated in a basis of configurations built from the one-electron orbitals. The number of two-electron configurations is typically 100 for uncoupled continuum states, and 500 for bound and AIS states, and includes angular momenta up to $l=4$. The bound state wave functions were calculated using the same one-electron basis as the continuum states.

The angular distribution of the ejected electrons is a further test of our calculations. Upon coupling the wave functions with the dipole operator, the angular part of the ejected electron distribution is given as

$$\begin{aligned}\frac{d\sigma_{L_\mu}}{d\Omega}=&\sum_{Ll}\sum_{L'l'}\sum_{m_l m_{l'}}\sum_{M_L M_{L'}}\sum_{KM_K M_\mu}(-1)^{l+l'+m_l+M_L+M'_{L'}}\\&\times\frac{\hat{K}\hat{L}\hat{L}'\hat{l}\hat{l}'}{\sqrt{4\pi}}\begin{pmatrix}K & l & l'\\ 0 & 0 & 0\end{pmatrix}\begin{pmatrix}K & l & l'\\ M_K & -m_l & m_{l'}\end{pmatrix}\\&\times\begin{pmatrix}l' & L_\mu & L'\\ m_{l'} & M_\mu & -M_{L'}\end{pmatrix}\begin{pmatrix}l & L_\mu & L\\ m_l & M_\mu & -M_L\end{pmatrix}\\&\times Y_K^{M_K}(\theta)(M^{LM_L}_{L_\mu kl})^* M^{L'M'_L}_{L_\mu kl'}.\end{aligned} \tag{9}$$

$L(L')$ and $M_L(M'_{L'})$ and are associated to the total angular

momentum of the final state, $L_\mu$ and $M_\mu$ refer to the angular momentum of the ion, and $L_i$ to the initial state of the atom. $Y_K^{M_K}(\theta)$ is the spherical harmonic and $\theta$ is the angle with respect to the polarization, $(M_{L_\mu kl}^{LM_L})$ is the amplitude of the multiphoton dipole transition from the initial state to a final continuum state with total angular momentum $L,M_L$. The latter state is associated to an ion with angular momentum $L_\mu$ and an ejected electron with angular momentum $l(l')$. Also, we use the notation $\hat{X}=\sqrt{2X+1}$. We use the dipole approximation, and we assume that the recoil of the atom is negligible. We also assume that the initial state has $M_i=0$ and that photons are linearly polarized with parallel polarizations. In this case, $M_L=M_{L'}=0$ and $M_K=0$, so that the cross section can be written

$$\frac{d\sigma_{L_\mu}}{d\Omega}=\sum_{Ll}\sum_{L'l'}\sum_{K}(-1)^{L_\mu}\frac{\hat{K}^2\hat{L}\hat{L}'\hat{l}\hat{l}'}{4\pi}\begin{pmatrix}K & l & l'\\ 0 & 0 & 0\end{pmatrix}\times\begin{pmatrix}K & L & L'\\ 0 & 0 & 0\end{pmatrix}\begin{Bmatrix}L' & L & K\\ l & l' & L_\mu\end{Bmatrix}P_K(\cos\theta)\times(M_{L_\mu kl}^{LM_L})^* M_{L_\mu kl'}^{L'M_{L'}'} \tag{10}$$

which is identical to Eq. (30) in Ref. [27]. The assumption that $M_i=0$ is fully justified in the case of three-photon ionization from the ground state since $L_i=0$. In this, our treatment differs from that of Ref. [5], where the population of all $M_i$ states is assumed and the angular distributions may be described with $N-1$ beta parameters for an $N$-photon process. However, our assumption should be treated carefully in the case of the two-photon ionization from the $3\,^1P(3s3p)$ state. In the experiment of interest [1], the polarization of the two colors of photons were not parallel, so this calculation is not strictly applicable to the experiment, but it has the advantage of being directly comparable to the three-photon ionization results. The angular distributions may then be written as a series of $\beta_K$ parameters:

$$\frac{d\sigma_{L_\mu}}{d\Omega}=\alpha_0\sum_K\beta_K P_K(\cos\theta), \tag{11}$$

where

$$\alpha_0=\frac{\sigma_{L_\mu}}{4\pi} \tag{12}$$

and $\sigma_{L_\mu}$ is the integrated cross section that corresponds to leaving the ion in the $L_\mu$ channel. This sum only includes even values of the $K$ index.

The beta parameters, for the case where $L_i=1$, $M_i=0$, and the ion is left in the $3s$ state are given by

$$\alpha_0=\frac{1}{4\pi}(|M_{3skp}^{10}|^2+|M_{3skf}^{30}|^2), \tag{13}$$

$$\alpha_0\beta_2=2|M_{3skp}^{10}|^2+\frac{4}{3}|M_{3skf}^{30}|^2+\frac{6\sqrt{21}}{7}\mathrm{Re}\{M_{3skp}^{10}(M_{3skf}^{30})^*\}, \tag{14}$$

$$\alpha_0\beta_4=\frac{18}{11}|M_{3skf}^{30}|^2+\frac{8\sqrt{21}}{7}\mathrm{Re}\{M_{3skp}^{10}(M_{3skf}^{30})^*\}, \tag{15}$$

$$\alpha_0\beta_6=\frac{100}{33}|M_{3skf}^{30}|^2. \tag{16}$$

For the case where the core is left in the $3p$ state, the $\beta$ parameters are given by

$$\alpha_0=\frac{1}{4\pi}(|M_{3pks}^{10}|^2+|M_{3pkd}^{10}|^2+|M_{3pkd}^{30}|^2+|M_{3pkg}^{30}|^2), \tag{17}$$

$$\begin{aligned}\alpha_0\beta_2=&|M_{3pkd}^{10}|^2+\frac{8}{7}|M_{3pkd}^{30}|^2+\frac{25}{21}|M_{3pkg}^{30}|^2\\&-2\sqrt{2}\,\mathrm{Re}\{M_{3pks}^{10}(M_{3pkd}^{10})^*\}\\&+2\sqrt{3}\,\mathrm{Re}\{M_{3pks}^{10}(M_{3pkd}^{30})^*\}\\&+\frac{18\sqrt{2}}{7}\mathrm{Re}\{M_{3pkd}^{10}(M_{3pkg}^{30})^*\}\\&-\frac{2\sqrt{6}}{7}\mathrm{Re}\{M_{3pkd}^{10}(M_{3pkd}^{30})^*\}\\&-\frac{4}{7\sqrt{3}}\mathrm{Re}\{M_{3pkd}^{30}(M_{3pkg}^{30})^*\},\end{aligned} \tag{18}$$

$$\begin{aligned}\alpha_0\beta_4=&\frac{6}{7}|M_{3pkd}^{30}|^2+\frac{81}{77}|M_{3pkg}^{30}|^2-4\,\mathrm{Re}\{M_{3pks}^{10}(M_{3pkg}^{30})^*\}\\&-\frac{12\sqrt{6}}{7}\mathrm{Re}\{M_{3pkd}^{10}(M_{3pkd}^{30})^*\}\\&+\frac{10\sqrt{2}}{7}\mathrm{Re}\{M_{3pkd}^{10}(M_{3pkg}^{30})^*\}\\&-\frac{60\sqrt{3}}{77}\mathrm{Re}\{M_{3pkd}^{30}(M_{3pkg}^{30})^*\},\end{aligned} \tag{19}$$

$$\alpha_0\beta_6=\frac{25}{33}|M_{3pkg}^{30}|^2-\frac{100\sqrt{3}}{33}\mathrm{Re}\{M_{3pkd}^{30}(M_{3pkg}^{30})^*\}. \tag{20}$$

## III. RESULTS

We have calculated three-photon cross sections from the ground state for the energy region between the $Mg^+$ $(3p)$ and the $Mg^+$ $(4s)$ thresholds. For the three-photon one-color ionization, process (A), the photon energy ranges between 0.145 and 0.2 a.u. (3.95–5.44 eV). The two-photon process

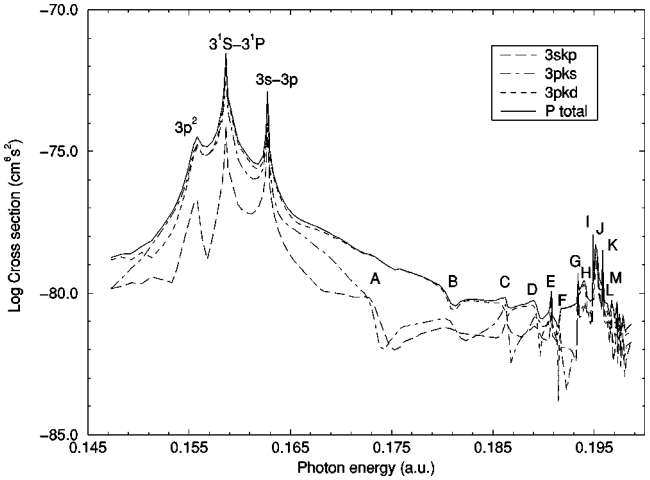


FIG. 2. Process (A) cross sections where $L=1$. The resonances are identified as follows: $A$: $4s4pB$: $3d4pC$ : $4s6pD$ : $3d6pE$ : $4s7pF$ : $3d5fG$ : $4s8pH$ : $3d7pI$:$4s10pJ$:$3d7fK$:$4s11pL$:$4s12pM$:$3d8f$.

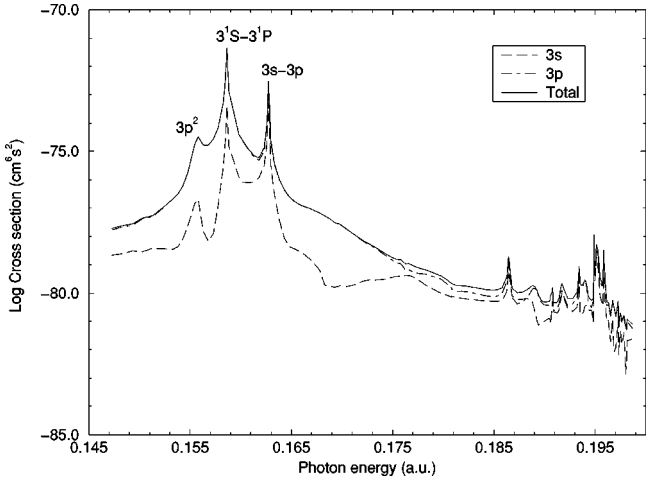


FIG. 4. Process (A) cross sections for the case where the ion is left in the $3s$ state, the $3p$ state, and the total ionization cross section.

from the $3\,^1P(3s3p)$ state, process (B), requires a photon energy of 0.145 and 0.22 a.u. (3.95–5.99 eV). The $3skp\ ^1P^o$, $3pks\ ^1P^o$, $3pkd\ ^1P^o$, $3skf\ ^1F^o$, $3pkd\ ^1F^o$, and $3pkg\ ^1F^o$ channels are open. Also $4skl$, $4pkl$, and $3dkl$ doubly excited states may be populated. We used 546 configurations to find a ground-state energy of $-0.830\,959$ a.u. with respect to the $Mg^{2+}$ ion. Our calculation of the $3\,^1P$ state used 313 configurations and found and energy of $-0.672\,350\,8$ a.u. The experimental values for these energy levels are $-0.833\,522$ and $-0.673\,816$. For the doubly excited states, 582 configurations were used in the$^1P^o$ symmetry, and 677 configurations were used for the$^1F^o$ symmetry. The cutoff parameter of the model potential was modified to obtain accurate energy values for the one-electron wave functions. The discrepancies between the experimental and theoretical energies are most likely due to the core potential. The cross sections for the $L=1$ case from the ground state is plotted in Fig. 2. The $L=3$ case from the ground state is plotted in Fig. 3, and total cross sections are shown in Fig. 4. In Fig. 4, $\sigma(3s)=\sigma(3skp)+\sigma(3skf)$ and $\sigma(3p)=\sigma(3pks)+\sigma(3pkd\ ^1P^o)+\sigma(3pkd\ ^1F^o)+\sigma(3pkg)$ are plotted.

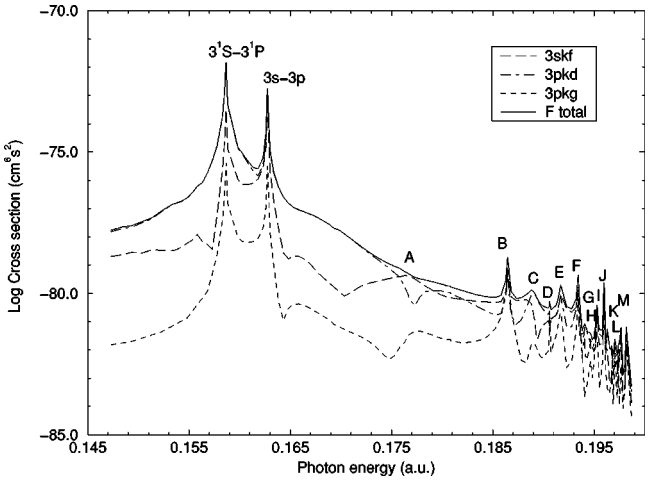


FIG. 3. Process (A) cross sections where $L=3$. The resonances are identified as follows: $A$:$3d4pB$:$4s4fC$:$3d6pD$:$3d5fE$: $4s6fF$: $4s7fG$:$3d7pH$:$3d6fI$: $4s9fJ$:$4s10fK$: $3d8pL$:$4s11fM$: $4s12f$.

The $L=1$ results for process (A) are dominated at low energies by (i) a bound-bound resonance, (ii) an AIS in the intermediate state, and (iii) a core excitation process. The higher energy region is dominated by a series of doubly excited states. In the low-energy region of the plot, the $3pks$ and $3pkd\ ^1P^o$ channels have the highest cross sections and at higher energies, the $3pkd\ ^1P^o$ channel has the largest cross section. The $3p^2\ ^1S^e$ AIS is populated by a two-photon process (see Fig. 2) and is the source of the lowest energy resonance at a photon energy of 0.153 a.u. At about 0.16 a.u., the $3\,^1S(3s^2)\rightarrow 3\,^1P(3s3p)$ bound-bound transition causes a singularity in the cross section. The case where this state is populated is presented later in the paper. The third resonance, at 0.164 a.u. is caused by a core excitation. This is the transition from the $3s$ to the $3p$ states in the $Mg^+$ ion. This excited state then couples with the continuum of the ejected electron and results in a resonance in the ATI cross section. The proximity of three resonances, the $3p^2\ ^1S^e$, the $3\,^1S(3s^2)\rightarrow 3\,^1P(3s3p)$ transition, and the core resonance makes the ATI cross section in the low-energy region unusually large. The height of the latter three peaks is infinite due to the breakdown of perturbation theory (PT). Nonperturbative approaches must be used to obtain ionization probabilities in the vicinity of these three resonances. The most common approaches are the direct solution of the time-dependent Schrödinger equation (TDSE) (see Ref. [20], Chap. 5), the density-matrix approach (see Refs. [12] and [13]) and the resolvent operator formalism. Note that the problem of the core excitation has been treated in detail in the latter approach by Hanson *et al.* [28]. In our problem, considering that the laser intensity is too low to significantly modify the positions and widths of the resonant states and that the band-

TABLE I. A comparison of the position, width, and assignment of doubly excited states and the photon energies required to populate the AIS. All energies are in a.u. Numbers in brackets denote powers of 10.

| $^1P^o$ resonances | | | | | |
|---|---|---|---|---|---|
| Label | Conf. | Energy | Width | Photon (A) | Photon (B) |
| *A* | $4s4p$ | −0.312 05 | 5.26[-3] | 0.172 97 | 0.180 15 |
| *B* | $3d4p$ | −0.288 50 | 5.40[-3] | 0.180 82 | 0.191 93 |
| *C* | $4s6p$ | −0.272 13 | 1.11[-3] | 0.186 28 | 0.200 11 |
| *D* | $3d6p$ | −0.263 03 | 2.46[-3] | 0.189 31 | 0.204 66 |
| *E* | $4s7p$ | −0.258 54 | 2.73[-4] | 0.190 81 | 0.206 91 |
| *F* | $3d5f$ | −0.256 13 | 9.70[-4] | 0.191 61 | 0.208 11 |
| *G* | $4s8p$ | −0.250 71 | 9.03[-5] | 0.193 42 | 0.210 82 |
| *H* | $3d7p$ | −0.247 87 | 1.30[-3] | 0.194 36 | 0.212 24 |
| *I* | $4s10p$ | −0.246 28 | 1.65[-5] | 0.194 89 | 0.213 04 |
| *J* | $3d7f$ | −0.244 58 | 1.70[-3] | 0.195 46 | 0.213 89 |
| *K* | $4s11p$ | −0.243 46 | 1.54[-5] | 0.195 83 | 0.214 45 |
| *L* | $4s12p$ | −0.241 56 | 5.33[-5] | 0.196 47 | 0.215 40 |
| *M* | $3d8f$ | −0.240 71 | 3.49[-4] | 0.196 75 | 0.215 82 |
| *N* | $4s13p$ | −0.240 10 | 4.48[-5] | 0.196 95 | 0.216 12 |
| *O* | $4s14p$ | −0.239 11 | 2.38[-5] | 0.197 28 | 0.216 62 |

| $^1F^o$ resonances | | | | | |
|---|---|---|---|---|---|
| Label | Conf. | Energy | Width | Photon (A) | Photon (B) |
| *A* | $3d4p$ | −0.299 70 | 1.06[-2] | 0.177 09 | 0.186 33 |
| *B* | $4s4f$ | −0.271 49 | 4.15[-4] | 0.186 49 | 0.200 43 |
| *C* | $3d6p$ | −0.264 13 | 2.91[-3] | 0.188 94 | 0.204 11 |
| *D* | $3d5f$ | −0.259 09 | 6.47[-5] | 0.190 62 | 0.206 63 |
| *E* | $4s6f$ | −0.255 81 | 9.55[-5] | 0.191 72 | 0.208 27 |
| *F* | $4s7f$ | −0.250 59 | 3.34[-4] | 0.193 46 | 0.210 88 |
| *G* | $3d7p$ | −0.248 80 | 9.59[-4] | 0.194 05 | 0.211 77 |
| *H* | $3d6f$ | −0.246 90 | 2.53[-4] | 0.194 69 | 0.212 73 |
| *I* | $4s9f$ | −0.245 13 | 3.43[-4] | 0.195 28 | 0.213 61 |
| *J* | $4s10f$ | −0.242 97 | 6.06[-5] | 0.196 00 | 0.214 69 |
| *K* | $3d8p$ | −0.242 03 | 6.84[-4] | 0.196 31 | 0.215 16 |
| *L* | $4s11f$ | −0.241 01 | 2.01[-5] | 0.196 65 | 0.215 67 |
| *M* | $4s12f$ | −0.240 43 | 3.51[-4] | 0.196 84 | 0.215 96 |
| *N* | $4s13f$ | −0.238 74 | 1.16[-4] | 0.197 41 | 0.216 81 |

width is narrow, the PT should be valid as long as the detuning at the resonance is larger than the autoionizing or natural width of the intermediate state. The remaining resonances are due to doubly excited AIS. The position and widths of the Feshbach states are shown in Table I, and the dominant configurations are listed in Table II. The $4s4p$ doubly excited singlet state produces a pronounced transparency in the $3skp$ and $3pks$ $^1P^o$ channels at 0.173 a.u., although it has little effect on the dominant $3pkd$ $^1P^o$ channel. The next lowest energy $^1P^o$ AIS, $3d4p$ induces a transparency in the $3pkd$ $^1P^o$ channel, while causing a peak in the $3skp$ and $3pks$ channels.

The $L=3$ results for process (A), shown in Fig. 3, are likewise dominated by the resonant $3\,^1S(3s^2)$ $\rightarrow 3\,^1P(3s3p)$ transition in the first photon, and the core excitation process. The $3pkd$ $^1F^o$ channel is the dominant channel in the low-energy region, while in the higher energy region, the $3skf$ and $3pkd$ $^1F^o$ channels have the largest cross sections. The high angular momentum $3pkg$ $^1F^o$ channel has a significantly lower cross section than all other channels. The selection rules require that the intermediate state have $L=2$, so the $3p^2$ $^1S^e$ AIS is not present in the $^1F^o$ channels. There are no Feshbach states in the region of interest in the intermediate $3skd$ channel. The high-energy region is also dominated by a large number of Feshbach states. The energy positions and widths of the Feshbach states are listed in Table I, and the significant configurations and amplitudes of these states are listed in Table II. The $3\,^1P(3s3p)$ singularity is present at 0.16 a.u., and the core resonance is again found at 0.164 a.u. The lowest energy $^1F^o$ AIS is the $3d4p$ state at 0.177 a.u. The state produces a transparency in the $3pkd$ $^1F^o$ channel and peaks in the $3skf$ and $3pkg$ channels. The $4s4f$ AIS at a photon energy of 0.186 a.u. produces a sharp resonance.

TABLE II. A list of the significant configurations contributing to each doubly excited state and its amplitude.

| $^1P^o$ symmetry | | | $^1F^o$ Symmetry | | |
|---|---|---|---|---|---|
| Label | Conf. | Amplitude | Label | Conf. | Amplitude |
| *A* | $4s4p$ | 0.73 | *A* | $3d4p$ | 0.81 |
| | $3d4p$ | −0.55 | | $3d5p$ | −0.40 |
| | $4s5p$ | −0.26 | | $4s4f$ | 0.38 |
| *B* | $3d4p$ | 0.56 | *B* | $4s4f$ | 0.64 |
| | $4s5p$ | −0.54 | | $4s5f$ | −0.50 |
| | $4s4p$ | 0.34 | | $3d5p$ | 0.44 |
| *C* | $4s6p$ | −0.59 | *C* | $3d6p$ | 0.57 |
| | $4s5p$ | 0.54 | | $3d5p$ | −0.51 |
| | $3d5p$ | −0.41 | | $4s5f$ | −0.44 |
| *D* | $3d5p$ | −0.50 | *D* | $3d5f$ | −0.67 |
| | $3d4f$ | −0.39 | | $3d4f$ | 0.55 |
| | $4s6p$ | 0.3 | | $4s6f$ | 0.3 |
| *E* | $4s7p$ | 0.63 | *E* | $4s6f$ | 0.67 |
| | $4s6p$ | 0.39 | | $3d6p$ | −0.40 |
| | $3d5f$ | −0.39 | | $4s7f$ | −0.34 |
| *F* | $3d5f$ | 0.54 | *F* | $4s7f$ | 0.60 |
| | $3d6p$ | −0.45 | | $3d7p$ | −0.52 |
| | $4s7p$ | −0.42 | | $4s8f$ | 0.34 |
| *G* | $4s8p$ | 0.79 | *G* | $3d7p$ | 0.48 |
| | $4s9p$ | −0.35 | | $3d6f$ | 0.45 |
| | $4s6p$ | −0.30 | | $4s8f$ | 0.43 |
| *H* | $3d7p$ | −0.59 | *H* | $3d6f$ | −0.60 |
| | $3d6f$ | −0.50 | | $4s7f$ | 0.43 |
| | $3d6p$ | 0.30 | | $4s10f$ | 0.40 |
| *I* | $4s9p$ | 0.71 | *I* | $4s9f$ | 0.67 |
| | $4s10p$ | −0.52 | | $4s7f$ | −0.33 |
| *J* | $3d7f$ | 0.53 | | $4s10f$ | −0.31 |
| | $3d6f$ | −0.5 | *J* | $4s10f$ | 0.65 |
| | $3d7p$ | 0.39 | | $3d8p$ | −0.41 |
| *K* | $4s11p$ | 0.65 | | $4s11f$ | −0.36 |
| | $4s10p$ | −0.54 | *K* | $3d8p$ | −0.53 |
| | $4s9p$ | −0.29 | | $4s11f$ | 0.41 |
| *L* | $4s12p$ | 0.69 | | $3d9p$ | 0.37 |
| | $4s10p$ | −0.36 | *L* | $4s11f$ | −0.47 |
| | $4s11p$ | −0.32 | | $3d8f$ | 0.47 |
| *M* | $3d8f$ | 0.61 | | $4s12f$ | −0.44 |
| | $3d7f$ | −0.42 | | $3d7f$ | 0.38 |
| | $4s13p$ | −0.29 | *M* | $4s12f$ | −0.52 |
| *N* | $4s13p$ | 0.64 | | $3d8f$ | 0.43 |
| | $4s14p$ | 0.50 | | $4s13f$ | 0.32 |
| | $4s11p$ | −0.32 | *N* 26 | $4s13f$ | 0.66 |
| *O* | $4s15p$ | −0.59 | | $4s14f$ | −0.42 |
| | $4s14p$ | 0.56 | | $4s11f$ | −0.36 |
| *P* | $4s16p$ | 0.55 | | | |
| | $4s15p$ | −0.50 | | | |

The total cross sections are plotted in Fig. 4. It should be noted that the total cross section of the $3p$ channels are higher than the $3s$ channels at all energies, and at lower energies the $3p$ channels generally have a cross section which is an order of magnitude higher.

The angular distributions for process (A) where the $Mg^+$ ion is left the in $3s$ state is plotted in Fig. 5, and the case where the ion is left in the $3p$ state is plotted in Fig. 6. Figure 5 shows that the angular distributions are anisotropic. Although the anisotropy seems to decrease markedly at the

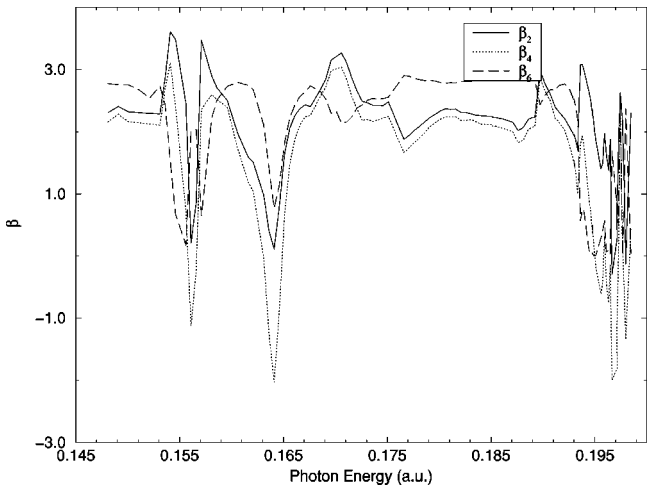


FIG. 5. Angular distributions for process (A), where the ion is left in the $3s$ state.

$3p^2\ ^1S^e$ AIS and the core excitation in the $3s$ channels, this must be taken with some caution because, as mentioned above, perturbation theory breaks down in the vicinity of these resonances. Figure 6 shows the angular distribution of electrons where the ion is left in the $3p$ state. The low cross section for the $3pkg$ channel results in a small $\beta_6$ parameter. The $\beta_4$ parameter is generally the largest contributor, although at the $3p^2\ ^1S^e$ resonance, it decreases sharply. At this resonance, both $\beta_4$ and $\beta_6$ approach zero, so that the distribution of electrons for much of the energy range would be strikingly similar to a $p$ wave.

Two-photon ATI cross sections from the $3\,^1P(3s3p)$ state, process (B), are now considered. This is the equivalent to the two-color experiment in which the $3\,^1S(3s^2)$ $\rightarrow 3\,^1P(3s3p)$ transition is pumped, followed by a second color photon to ionize the atom. We are, in effect, looking at the case where the intensity of the nonresonant color is much greater than the intensity of the resonant color.

In Fig. 7, we consider the $L=1$ case for process (B). At

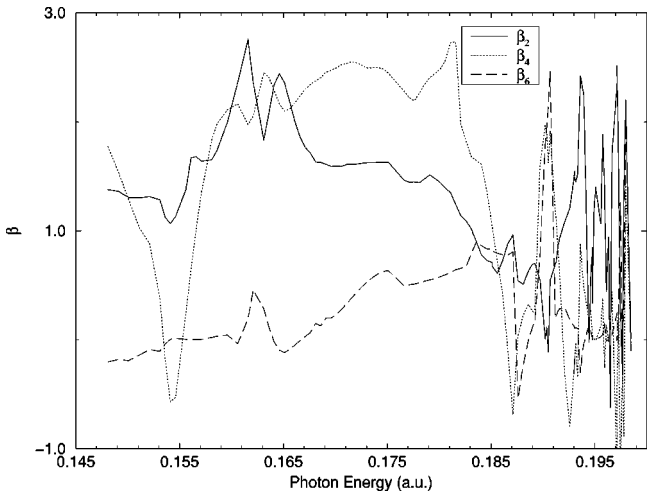


FIG. 6. Angular distributions for process (A), where the ion is left in the $3p$ state.

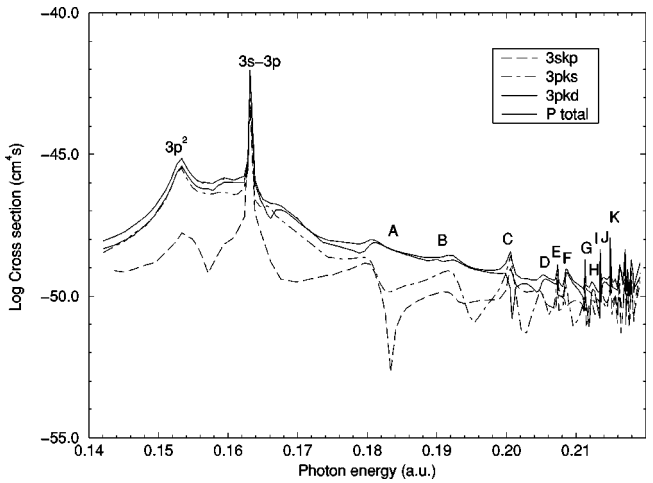


FIG. 7. Process (B) cross sections, where $L=1$. The resonances are identified as follows: $A$:$4s4pB$:$3d4pC$:$4s6pD$:$3d6pE$ : $4s7p$ $F$: $3d5fG$:$4s8pH$ : $3d7pI$ : $4s10pJ$ : $3d7fK$:$4s11pL$:$4s12pM$:$3d8f$.

lower energies, the $3pkd$ and $3pks$ $^1P^o$ channels have the greatest cross sections, and at higher energies, the $3pkd$ channel dominates. Once again, the low-energy region is dominated by the $3p^2\ ^1S^e$ AIS in the intermediate state at a photon energy of 0.153 a.u., and the core excitation resonance at 0.16 a.u. At higher energies, the same Feshbach states that occur in the three-photon problem are present. The $4s4p$ AIS produces a transparency in the $3skp$ and $3pks$ channels, and a peak in the $3pkd\ ^1P^o$ channel. The $3d4p\ ^1P^o$ AIS causes a resonance in all channels at 0.192 a.u. At higher energies, there is a large number of AIS states whose positions and widths are cataloged in Table I, and their dominant configurations are listed in Table II.

In Fig. 8, we consider the $L=3$ channels for process (B). The $3pkd\ ^1F^o$ channel has the largest cross section and the high angular momentum $3pkg$ channel has by far the lowest

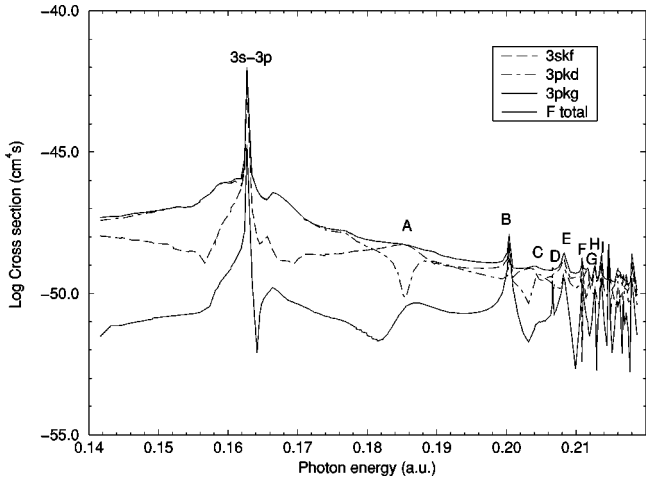


FIG. 8. Process (B) cross sections, where $L=3$. The resonances are identified as follows: $A$:$3d4pB$:$4s4fC$:$3d6pD$:$3d5fE$:$4s6fF$:$4s7fG$:$3d7pH$ : $3d6fI$:$4s9fJ$:$4s10fK$:$3d8pL$:$4s11fM$:$4s12f$.

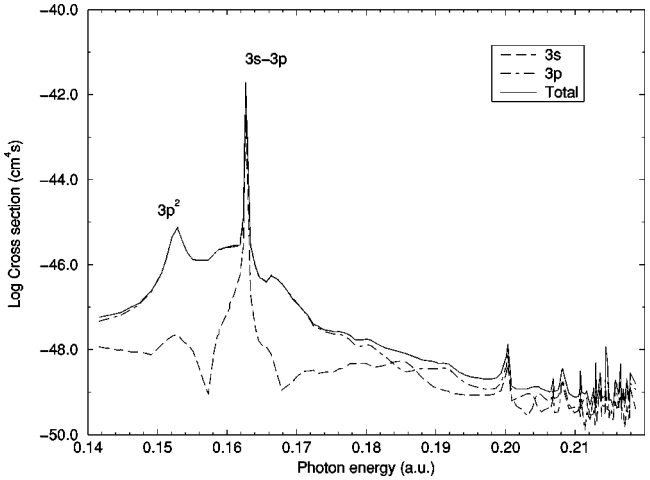


FIG. 9. Process (B) cross sections, where the ion is left in the $3s$ state, the $3p$ state, and the total ionization cross sections.

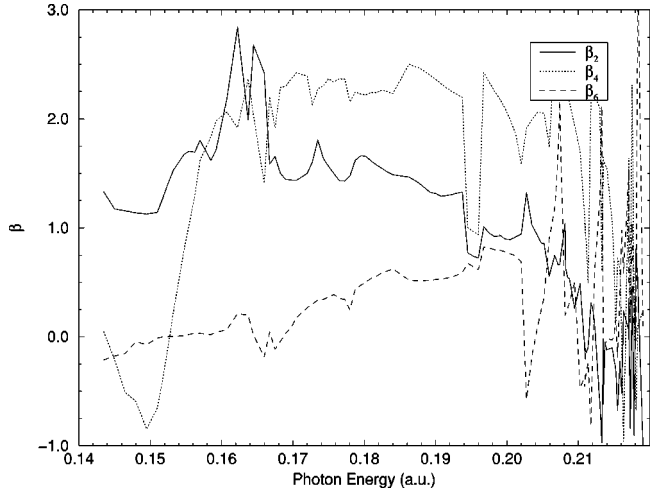


FIG. 11. Angular distributions for process (B), where the ion is left in the $3p$ state.

cross section of the channels. The low-energy region is relatively featureless, except for the presence of the core excitation. The lowest energy AIS, the $3d4p\,^1F^o$, is at 0.186 a.u. and causes a transparency in the $3pkd$ channel, and resonances in the $3skf$ and $3pkg$ channels. The $4s4f$ AIS at 0.200 a.u. causes a striking peak in all channels.

In Fig. 9, the process (B) total cross sections are plotted as a function of energy. The $3p$ channels again have far larger cross sections than the $3s$ channels. It is worth noting the large differences between the calculated cross sections, and the experimental cross sections found by Darveau and Berry. These experiments found a cross section, from the $3\,^1P(3s3p)$ state to be $1.42\pm0.096\times10^{-43}$ cm$^4$ s, while we found a cross section of about $1.2\times10^{-48}$ cm$^4$ s at 0.1542 a.u., the corresponding energy. While ATI cross sections are very difficult to determine experimentally, this difference is large enough to be quite significant. In principle, the main difficulty in comparing these two numbers is that the composition of the experimental signal is difficult to determine. It may be attributed to either an ATI process, or to a scattering process. Further experiments by the group have concluded that the exponent of the dependence of this peak on the Mg density is actually 2, which implies that the dominant mechanism in this peak is a superelastic scattering process. The electrons are ejected by a REMPI process, and the ejected electron interacts with a second excited Mg atom, and during the resulting collision the atom de-excites to the ground state, transferring the excess energy to the electron. These calculations support the conclusion that the high-energy electrons produced in the experiments of Darveau and Berry are caused by a superelastic collision between a photoelectron and an excited Mg atom. Further experiments will be reported to confirm this.

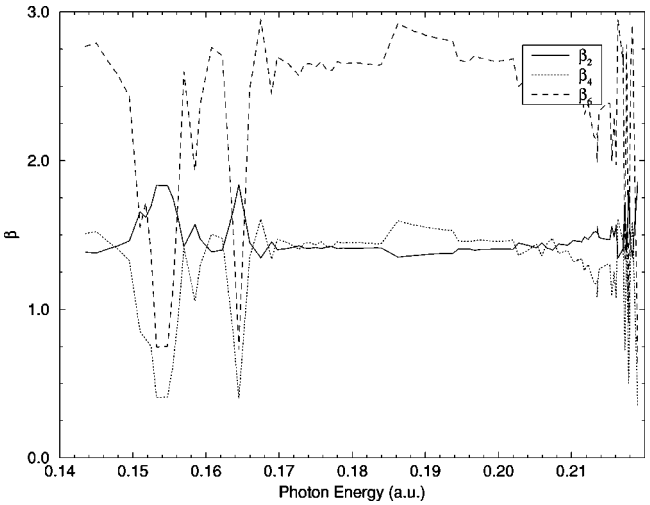


FIG. 10. Angular distributions for process (B), where the ion is left in the $3s$ state.

In Figs. 10 and 11, we show the angular distribution of the ejected electrons for process (B) where the ion is left in the $3s$ and $3p$ state, respectively. In the $3s$ case, the $\beta_6$ parameter is much larger than the $\beta_2$ and $\beta_4$ parameters throughout most of the spectrum. The $3p^2\ ^1S$ AIS causes the $\beta_4$ and $\beta_6$ parameters to approach zero, so the distribution is similar to a $p$ wave. The core excitation also makes the distribution to roughly approach a $p$ wave. The $3p4d$ AIS at 0.186 a.u. causes the $\beta_4$ to become the dominant term of the beta parameters. In the $3p$ case, the $\beta_6$ is quite small throughout due to the relatively low cross section of the $3pkg$ channel.

## IV. CONCLUSIONS

We have studied the three-photon ionization and the two-photon ionization from the $3\,^1P(3s3p)$ state of Mg between the $3p$ and $4s$ threshold using an $L^2$ integrable $B$-spline basis in the Feshbach formalism. This system is ideal for experimental studies due to the presence of three significant resonances, the population of the $3\,^1P(3s3p)$ state, the $3p^2\ ^1S^e$ state in the intermediate state, and the core excitation. Because of the proximity of these three resonances, the cross section for ATI in this region is unusually high. Also, the

photon energy required to observe these resonances are accessible by many laser systems. We also report the positions, widths, and configurations of a number $L=1$ and $L=3$ AIS which lie between the $3p$ and $4s$ thresholds. We have also helped to confirm the identity of the signal in Darveau and Berry [1] as most likely being predominantly due to superelastic collisions. Furthermore, we would like to support future experiments, especially in the region of the core excitation and the bound-bound resonance.

**ACKNOWLEDGMENTS**

The authors would like to thank Tahllee Baynard and Scott Darveau for useful discussions and experimental motivation. This work was supported by the National Science Foundation, the Department of Education, the Ministerio de Ciencia y Tecnología, and the Comisión de Intercambio Cultural, Educativo y Científico Entre España y los Estados Unidos de América.

[1] S. Darveau and R.S. Berry, *Resonance Ionization Spectroscopy* (AIP, Woodbury, NY, 1998).
[2] P. Agostini, F. Fabre, G. Mainfray, G. Petite, and N.K. Rahman, Phys. Rev. Lett. **42**, 1127 (1979).
[3] P. Kruit and F.H. Read, J. Phys. E **16**, 313 (1983).
[4] I. Sánchez, H. Bachau, and F. Martín, J. Phys. B **30**, 2417 (1997).
[5] R. Moccia and P. Spizzo, J. Phys. B **21**, 1121 (1988).
[6] R. Moccia and P. Spizzo, J. Phys. B **21**, 1133 (1988).
[7] R. Moccia and P. Spizzo, J. Phys. B **21**, 1145 (1988).
[8] S. Mengali and R. Moccia, J. Phys. B **29**, 1597 (1996).
[9] S. Mengali and R. Moccia, J. Phys. B **29**, 1613 (1996).
[10] N.J. Kylstra, H.W. van der Hart, P.G. Burke, and C.J. Joachain, J. Phys. B **31**, 3089 (1998).
[11] E. Luc-Koenig, A. Lyras, J.M. Lecomte, and M. Aymar, J. Phys. B **30**, 5213 (1997).
[12] N.E. Karapanagioti, O. Faucher, Y.L. Shao, D. Charalambidis, H. Bachau, and E. Cormier, Phys. Rev. Lett. **74**, 2431 (1995).
[13] N.E. Karapanagioti, D. Charalambidis, C.J.G.J. Uiterwaal, C. Fotakis, H. Bachau, I. Sánchez, and E. Cormier, Phys. Rev. A **53**, 2587 (1996).
[14] T.N. Chang and X. Tang, Phys. Rev. A **46**, R2209 (1992).
[15] A. Reber, F. Martín, H. Bachau, and R.S. Berry, Phys. Rev. A **65**, 063413 (2002).
[16] R.E. Bonanno, C.W. Clark, and T.B. Lucatorto, Phys. Rev. A **34**, 2082 (1986).
[17] Y.L. Shao, C. Fotakis, and D. Charalambidis, Phys. Rev. A **48**, 3636 (1993).
[18] A. Lyras and H. Bachau, Phys. Rev. A **60**, 4781 (1999).
[19] C. De Boor, *A Practical Guide to Splines* (Springer, New York, 1978).
[20] H. Bachau, E. Cormier, P. Decleva, J. Hansen, and F. Martín, Rep. Prog. Phys. **64**, 1601 (2001).
[21] I. Sánchez and F. Martín, Phys. Rev. A **44**, 7318 (1991).
[22] M. Cortés and F. Martín, J. Phys. B **27**, 5741 (1994).
[23] H. Bachau, P. Lambropoulos, and X. Tang, Phys. Rev. A **42**, 5801 (1990).
[24] H. Feshbach, Ann. Phys. (N.Y.) **19**, 287 (1962).
[25] O.K. Rice, J. Chem. Phys. **1**, 375 (1933).
[26] R. Moccia and P. Spizzo, Phys. Rev. A **39**, 3855 (1989).
[27] C.R. Liu, N.Y. Du, and A.F. Starace, Phys. Rev. A **43**, 5891 (1991).
[28] L.G. Hanson, J. Zhang, and P. Lambropoulos, Phys. Rev. A **55**, 2232 (1997).